

Determination of local geometrical distortions in an ordered omphacite under high pressure

Lisa Baratelli^{1*}, Marco Merlini², Fabrizio Nestola³, Jacopo Nava³, Bobby Joseph⁴, Mauro Precipe⁵ and Fernando Cámara²

¹Department of Earth and Environmental Sciences, University of Pavia, Via Adolfo Ferrata 1, 27100 Pavia, Italy

²Department of Earth Sciences, University of Milan, Via Sandro Botticelli 23, 20133 Milan, Italy.

³Department of Geosciences, University of Padua, Via Giovanni Gradenigo 6, 35131 Padua, Italy.

⁴Elettra Sincrotrone, S.S. 14 – km 163.5 in AREA Science Park, 34149, Basovizza, Trieste, Italy.

⁵Department of Earth Sciences, University of Turin, Via Valperga Caluso 35, 10125 Turin, Italy

*Corresponding author: lisa.baratelli@unipv.it

Abstract

Single-crystal synchrotron X-ray diffraction data were collected on a natural omphacite with composition close to $Jd_{43}Di_{57}$, at the Xpress beamline at Elettra Synchrotron, up to 10 GPa at room temperature using a diamond anvil cell. A second-order Birch-Murnaghan equation of state fit to the unit-cell volumes determined at 20 pressure points yielded $V_0 = 422.85(15) \text{ \AA}^3$, and $K_0 = 121.3(1.2) \text{ GPa}$. These elastic parameters are consistent with the general trend of the diopside-jadeite join. The structural evolution with pressure was determined from

both *ab initio* simulations and structure refinements to the X-ray intensity data. The consistency between experimental findings and local geometrical distortions identified through *ab initio* calculations is discussed. A distortion variation at the *M1* polyhedron occurs around 3 GPa, which correlates with the TILT angle of the *T2* tetrahedron which stabilises at a similar pressure, coinciding with a decrease in the rate of *M1* deformation under pressure.

These results in the structural evolution with pressure correlate with the changes observed previously in some Raman shifts in the same pressure range in the same material.

Keywords: Omphacite; high-pressure; single-crystal XRD; synchrotron; equation of state

Introduction

Omphacite is a single-chain silicate characterized by the general formula $M1M2T_2O_6$, where *T* represents the tetrahedrally coordinated Si, and *M1* and *M2* denote six- and eight-coordinated sites, respectively. *M1* is typically occupied by high-charge small cations as Mg, Al, Cr, Mn, Fe^{2+} or Fe^{3+} , while large divalent or monovalent cations such as Ca, Na or Li, are present in *M2*. The cation ordering process in omphacite results in the splitting of the *M1* and *M2* sites into non-symmetrically related pairs: *M1* and *M11*, and *M2* and *M21*, respectively. The *M1* site is preferentially occupied by Al, *M11* by Mg, while *M21* is occupied by Na and *M22* by Ca. Consequently, the presence of cation order in the *M* sites lowers the space group symmetry from *C2/c* to *P2/n*.

A recent high-pressure (HP) Raman spectroscopy study of natural *P2/n* omphacite, with composition close to $Jd_{43}Di_{57}$, up to 10 GPa revealed some changes in the Raman shifts and full width at half maximum (FWHM) at some wavenumbers that may be interpreted as due to changes in its elastic behaviour (Baratelli *et al.*, 2024). In particular, the pressure dependence of the wavenumbers of a few Raman peaks changes around 5 GPa that could

indicate a change in the detailed compression mechanisms in the six- and eight-coordinated sites within the ordered omphacite structure.

Several studies have already investigated the compressional behaviour of ordered $P2/n$ and disordered $C2/c$ omphacite by using single crystal X-ray diffraction (SC-XRD) (McCormick *et al.*, 1989; Pavese *et al.*, 2001; Nishihara *et al.*, 2003; Pandolfo *et al.*, 2012a; b; Zhang *et al.*, 2016; Xu *et al.*, 2019; Ye *et al.*, 2022). Furthermore, the thermal behaviour of omphacite has also been investigated (Pavese *et al.*, 2000; Nishihara *et al.*, 2003; Pandolfo *et al.*, 2012b; Xu *et al.*, 2019; Ye *et al.*, 2022). Brillouin spectroscopy has been employed to determine the elastic properties of both disordered (Bhagat *et al.*, 1992) and ordered (Hao *et al.*, 2019) omphacite at room conditions and room-temperature high-pressure respectively.

Table 1 summarizes the isothermal equations of state (EoSs) for omphacite reported in the literature, in terms of bulk modulus (K_0), its pressure derivative (K'), the zero-pressure volume V_0 as well as the order parameters and the chemical composition. K_0 for ordered omphacite ranges between 116(2) and 122(1) GPa (Pavese *et al.*, 2001; Pandolfo *et al.*, 2012a; Zhang *et al.*, 2016), while for disordered omphacite it is 119(2) GPa (Pandolfo *et al.*, 2012b). McCormick *et al.* (1989) showed that vacancies in the M sites increase the compressibility. Table 1 includes thermal EoS parameters (Pavese *et al.*, 2000; Nishihara *et al.*, 2003; Pandolfo *et al.*, 2012b; Xu *et al.*, 2019; Ye *et al.*, 2022), in terms of the thermal expansion coefficient (α_V) and the temperature derivative of the bulk modulus ($\partial K_T/\partial T$), both at room conditions.

Despite these extensive studies, all of the HP structural studies published so far suffer from an incomplete exploration of reciprocal space that limits the refinement of the structure under variable pressure. In particular, the limited data coverage does not allow refinement of the anisotropic atomic displacement parameters (adp's) for all atoms in the omphacite

structure, that is necessary to follow accurately the geometrical changes with changing pressure. This limits the reliability of the structural parameters and thus the possible interpretation of results obtained by HP Raman spectroscopy. Moreover, the published HP studies of omphacites each contain only a limited number of pressure data points, and this means that subtle variations in compression mechanisms cannot be identified. To address these issues, we have conducted a HP SC-XRD study, on the same sample studied by Raman spectroscopy (Baratelli *et al.*, 2024), at the Xpress beamline of the Elettra Synchrotron in Trieste, focusing efforts on accessing as much of reciprocal space as possible and by collecting data at small intervals in pressure. The findings from this experimental study are compared with results from Hartree-Fock/Density Functional Theory (HF/DFT) simulations on a fully ordered $\text{Jd}_{50}\text{Di}_{50}$ omphacite up to 8 GPa and with the Raman spectra collected up to 10 GPa by Baratelli *et al.* (2024).

Materials and methods

Sample description

We used an omphacite crystal from the Münchberg Massif, Bavaria (Matthes and Schmidt, 1974; O'Brien, 1993), which belongs to the same omphacite sample (74AM41) that has been previously analysed by infrared spectroscopy and SC-XRD (Boffa Ballaran *et al.*, 1998a; b). The sample was selected for the low Fe content to avoid its effect on the Di-Jd solid solution and has the composition $(\text{Ca}_{0.57}\text{Na}_{0.43})(\text{Mg}_{0.50}\text{Al}_{0.43}\text{Fe}_{0.07})(\text{Si}_{1.96}\text{Al}_{0.04})\text{O}_6$ (Baratelli *et al.*, 2024). Refinement of SC-XRD data at room conditions allowed us to determine that the crystal exhibits extinction violations corresponding to the $P2/n$ space group.

Single-crystal X-ray diffraction (SC-XRD)

The structure of the selected omphacite crystal ($107 \times 131 \times 229 \mu\text{m}^3$) was determined by SC-XRD measurements at room temperature and ambient pressure using a Rigaku XtaLAB

Synergy-S diffractometer equipped with a HyPix-6000HE HPC area detector, at the Department of Earth Sciences of the University of Milan. A monochromatic X-ray incident beam with an energy of 17.4 keV ($\lambda=0.71073$ Å, *i.e.* MoK α) was used. The data collection strategy involved a stepwise ω -rotation in the range of $\pm 58^\circ$, with a step width of 0.5° , and an exposure time of 3.5 s per step. Structure refinements were performed using the SHELXL program (Sheldrick, 2015). The structure was refined in the $P2/n$ space group. Scattering curves were taken from The International Tables for Crystallography (Wilson, 1995). Neutral vs. ionized scattering factors were used to refine the occupancy of sites not involved in chemical substitutions (*i.e.* O sites and ^{71}Si in $P2/n$) (Hawthorne *et al.*, 1995), while ionized atoms scattering factors were used for ^{72}Si and the six- and eight-coordinated sites ($M1$, $M11$, $M2$, $M21$). The site partitioning (Table 2) was determined using the refinement model proposed by Boffa Ballaran *et al.* (1998a) and the chemical constraints from the EMPA data reported by Baratelli *et al.* (2024). The refinement converged to $R1 = 2.18\%$ for 2919 observed reflections with $I/\sigma > 4$ and 118 parameters (Table S1), yielding acceptable displacement parameters for all atoms. Atom fractional coordinates and displacement parameters are listed in Supplementary Tables S2 and S3, respectively.

Then the crystal was cut in two different perpendicular directions using a focused ion beam (FIB), to obtain two slices with dimensions ca. $50\times 50\times 30$ and $60\times 40\times 30$ μm^3 . The FIB cut was done with the FEG-FIB Tescan Solaris at the Department of Geosciences of the University of Padova. This was intended to overcome the limitations in accessibility to reciprocal space in standard HP studies with diamond-anvil cell (DAC) with only one crystal of low symmetry. This procedure enabled us to collect 57% of the reflections in one asymmetric unit at a resolution of $d = 1.081$ Å, while $\sim 30\%$ coverage was achieved at a maximum resolution of 0.599 Å. The ratio of refined parameters (including adp's) to data was approximately 6.5.

The two omphacite slices were loaded in a BX-90 DAC. The pressure-transmitting medium used in this experiment was a mixture of methanol:ethanol in 4:1 proportions, which transmits pressure hydrostatically up to the maximum pressure reached in this experiment (Angel *et al.*, 2007; Klotz *et al.*, 2009). Ruby fluorescence was used as a pressure standard, and the estimated pressure uncertainty is about 0.05 GPa (Mao *et al.*, 1986). *In situ* HP SCXRD measurements were performed at the beamline Xpress of the Elettra synchrotron (Trieste, Italy). The data collection strategy involved a stepwise ω -rotation in the range of $\pm 32^\circ$, with a step width of 0.5° , and an exposure time of 0.5 s per step. The experimental setup featured a parallel monochromatic beam ($E = 25$ KeV, $\lambda = 0.49585$ Å), and diffraction patterns were collected by a PILATUS3 S 6M detector (from DECTRIS) flat-panel detector. The experiment was conducted up to 10 GPa, with a total of 24 pressure points (three of them on decreasing pressure) approximately equally spaced in pressure. The indexing of the diffraction data, unit-cell parameter refinement, and intensity integration were performed using the CrysAlisPro suite (Rigaku Oxford Diffraction, 2019). Semiempirical absorption (due to the DAC components) and background corrections were implemented using the ABSPACK routine implemented in the CrysAlisPro suite. The structural refinements for each HP point were handled with Jana2006 (20/02/2023 version) software (Petříček *et al.*, 2014). The reflection files of the two omphacite slices were used together with their own respective scale factors in a single refinement.

The values of the conventional agreement factor $R1$ as well as other details from every pressure step refinement are reported in Table S1.

Computational methods

Ab initio hybrid HF/DFT simulations have been conducted with the CRYSTAL17 software (Dovesi *et al.*, 2018) by using the WC1LYP functional. This functional has been

shown to correctly reproduce the elastic and vibrational properties of crystals (e.g. Prencipe et al. 2011, 2012; Prencipe 2012, 2019; Stangarone et al. 2016). The WC1LYP functional is based on the generalized gradient approximation exchange functional WC (Wu and Cohen, 2006), mixed with 16% of the exact *non-local* HF exchange, and the Lee-Yan-Parr (LYP) correlation functional (Lee et al., 1988). The grid for the numerical evaluation of the DFT exchange-correlation functionals was chosen by the keyword XLGRID of CRYSTAL17 (Dovesi et al., 2018) and corresponds to a total of 900,780 points in the unit cell. A measure of the numerical accuracy provided by such a grid is the evaluation of the total number of electrons in the unit cell, by the numerical integration of the electron density over the cell volume. For omphacite, we obtained 415.99999 electrons out of 416 for the reference volume at the static limit (no zero-point and thermal pressures due to vibrational effects included, see Prencipe et al. 2011) and at a static pressure of 0 GPa. The localized contracted atomic basis sets used were: Na 8-511(1d)G; Al 85-11(1d)G; Ca 865-11(3d)G; Mg 85-11(1d)G; Si 88-31(1d)G; O 84-11(1d1d)G (Valenzano et al., 2006; Sophia et al., 2014). Within the CRYSTAL code, the accuracy in evaluating the Coulomb and HF exchange series is controlled by the keyword TOLINTEG, for which we set the four T1, T2, T3 and T4 parameters to 9 and T5 to 22 (Dovesi et al., 2018). Diagonalization of the Hamiltonian matrix was performed at 30 independent k vectors in the reciprocal space (Monkhorst net; Monkhorst and Pack 1976) by setting the shrinking factor IS to 4 (Dovesi et al., 2018). Unit-cell parameters and fractional coordinates were optimized by analytical gradient methods, as implemented in CRYSTAL17 (Civalleri et al., 2001; Dovesi et al., 2018). Geometry optimization was considered converged when each component of the gradient (TOLDEG parameter in CRYSTAL17) was smaller than 0.00003 Hartree/Bohr and displacements (TOLDEX) were smaller than 0.00012 Bohr with respect to the previous step. Simulations of

the structure of omphacite at the *static limit* have been performed at pressures ranging from -2 to 8 GPa with a step of 1 GPa. In order to directly compare the computational data with the experimental results, we followed the procedure reported in Ghignone et al. (2024) to estimate the EoS parameters at a temperature of 298 K. These estimations are made at the static level (P_{static}) and do not account for the influence of atomic vibrations (P_{vib}) in the solid, which typically leads to a reduction in K_0 (Prencipe, 2019).

Results

Degree of order

The site populations determined by refinement to the diffraction data collected from the crystal in air (Table 2) were kept fixed in the structure refinements of diffraction data collected at HP, as it cannot change at room-temperature. The chemical constraints are derived from the chemical composition of sample 74AM41, which was studied by Boffa Ballaran et al. (1998a). This is the same rock sample to which the analysed crystal belongs. This site population was used to calculate the order parameters $Q^{\text{occ}}_{M1} = 0.83$ and $Q^{\text{occ}}_{M2} = 0.43$, whereas Q^{dist}_{M1} and Q^{dist}_{M2} reported in Table 2 were calculated from the average bond lengths obtained with the same model at room-pressure. Q^{occ} and Q^{dist} were calculated with the formulas reported by Carpenter et al. (1990a; b).

Unit-cell parameters and volume evolution with pressure

The unit-cell parameters and volume collected in air and at variable pressure conditions (21 pressure values and data collected up to 9.73 GPa, *i.e.* a pressure point every ca. 0.46 GPa) are reported in Table 3, as well as the ones from the *ab initio* simulations from -2 to 8 GPa. The unit-cell volume at ambient pressure (V_0) could not be determined at the Elettra Synchrotron because the crystals were loaded into the DAC prior to the start of the experiment. Fig. 1 illustrates the changes in the experimentally and HF/DFT calculated unit-

cell parameters with pressure. Fig. 2 shows the pressure dependence of the unit-cell volumes from both the experiment and HF/DFT calculations. A steady decrease of a , b , c , β angle, and volume, V , was observed as a function of pressure with no evidence of discontinuities or clear changes in slope related to a phase transition in the studied pressure range. The behaviour of the a and c cell parameters is quite similar. However, the b cell parameter exhibits a change in the experimentally collected data, beginning to decrease more around 4 GPa, indicating a softening, while the $a \cdot \sin(\beta)$ direction, which corresponds to the direction along which the tetrahedra chains extend, becomes stiffer. However, considering the *ab initio* data, the b cell parameter does not present any variation around 4 GPa, whereas it is confirmed that the $a \cdot \sin(\beta)$ direction is the stiffest. The scattering in the HP data presented in these graphs (in particular for the point at 9.13 GPa) can be attributed to the limitations of experimental geometry, which is not the best to obtain accurate cell parameter determinations (Angel *et al.*, 2000), but the overall trends are clearly discernible. One way to demonstrate the quality of the experimental data is the f_E - F_E plot (Angel, 2000) that shows the dependence of the Eulerian strain ($f_E = [(V_0/V)^{2/3}-1]/2$) on the normalised stress ($F_E = P/3 f_E (1-2f_E)^{5/2}$). Since the f_E - F_E plot requires knowledge of V_0 , which could not be measured, the selection of the EoS was based on the evaluation of the errors of the parameters, the goodness of fit and maximum misfit of pressure. Least-squares fits were weighted by the uncertainties of both pressure and volume in the EoSFit7-GUI software (Gonzalez-Platas *et al.*, 2016). A second-order Birch-Murnaghan (BM2) EoS fits the experimental data as well as a third-order BM EoS, while the refined value of K' for the BM3 EoS deviates by less than 1 estimated uncertainty from the implied value of 4 for the BM2 EoS. The refined parameters for a BM2 EoS are $V_0 = 422.85(15) \text{ \AA}^3$, and $K_0 = 121.3(1.2) \text{ GPa}$ (Table 4). The elastic parameters obtained are consistent with the general trends on the Di-

Jd join (see Table 1). In Fig. S1, the confidence ellipses were calculated for our samples and the datasets of ordered omphacite presented in Table 1, up to a confidence level of 68.3 %. A parameterised form of the BM2 EoS was used to determine the axial moduli of a , b , and c , and $a\sin\beta$ using EoSFit7-GUI with the data weighted by the uncertainties of both pressure and lattice parameters. The calculated EoS coefficients are reported in Table 4.

For the fully ordered $\text{Jd}_{50}\text{Di}_{50}$ omphacite, calculated with hybrid HF/DFT simulations, we employed a third-order Birch-Murnaghan EoS (BM3), and the fit of all data yields $V_0 = 426.52(3) \text{ \AA}^3$, $K_0 = 119(2) \text{ GPa}$, and $K' = 4.9(5)$ (Table 4).

Structure evolution with pressure

The fractional coordinates and displacement parameters obtained using the merged diffraction data of the two slices of the $\text{Jd}_{43}\text{Di}_{57}$ omphacite are reported in Tables S2 and S3, respectively, in the supplementary material. Bond lengths, specific angles, polyhedral volumes and deformation parameters are listed in Table S4 in the supplementary material. Table S5 reports the corresponding structural parameters calculated with HF/DFT simulations. The full structural data has also been deposited in crystallographic information files (CIFs) as supplementary materials.

T sites

Although tetrahedral sites in minerals are often considered to be rigid, a small decrease in volume (about 3.6%) of both the $T1$ and $T2$ sites up to the maximum pressure was measured (Table S4). Nevertheless, the silicon tetrahedra remain the stiffest polyhedra in the structure, with K_0 of 308(29) GPa for $T1$ and 257(21) GPa for $T2$, respectively. The TILT angle is defined as the out-of-plane tilting of the basal face of the tetrahedra with respect to the plane (100) (Cameron *et al.*, 1973), and it is related to the way the M and T polyhedra accommodate each other. Therefore it is sensitive to the ordering process (as these change

the M octahedra geometry; see Boffa Ballaran et al. 1998a and Cámara et al. 1998, for a description of the variation of TILT angle with cation order), but it is also sensitive to increasing pressure (Fig. 3a,b). As pressure is increased the tetrahedra basal faces tend to align parallel to the (100) plane. TILT of $T2$ (Fig. 3b), in particular, ceases to decrease around 3 GPa, and also *ab initio* simulations confirm that this angle starts to decrease slowly at about 3 GPa and remains almost constant at higher pressure. The $TILT_{az}$ represents the azimuthal component of the TILT angle (Boffa Ballaran et al., 1998a) for the two neighbouring tetrahedra $T1$ and $T2$. The $TILT_{az}$ of $T1$ decreases with pressure (Fig. 3c), but the experimental data show a significant scatter. $TILT_{az}$ of $T2$ is characterized by a stronger pressure dependence (Fig. 3d). Consequently, the changes in $TILT_{az}$ of $T2$ indicates that this tetrahedron continues to rotate even after it stops tilting.

The dihedral angle between the basal faces of the two tetrahedra (\hat{T}), which defines the bending of the chain of tetrahedra with respect to the c axis (see Fig. S2, supplementary material), increases with pressure, leading to a flattening of the chain towards the (100) plane.

M sites

From the variation of the observed polyhedral volumes (Table S4) it is observed that the smallest compressibility of the M sites in the structure is displayed by the octahedral polyhedra (5.6 % for $M1$ and 4.4% for $M11$). Fig. 4 shows the evolution of the polyhedral volumes for the M sites, compared to the ones calculated with *ab initio* simulations. The estimated standard uncertainties reported in Fig. 4a,b and in Table S4 were calculated using the Crystal Palace software (Angel et al., submitted). The eight-coordinated polyhedra ($M2$ and $M21$) are the most compressible (see Table 4) and contribute the most to the unit-cell compression (7.3 % for $M2$ and 7.8% for $M21$). A BM2 EoS weighted by the uncertainties of

both pressure and volume was fitted to polyhedral volume of M sites, while a BM3 EoS was used for the HF/DFT data. The results are reported in Table 4. Our data clearly shows the higher stiffness for the $M11$ site, as one can expect for a small octahedral site essentially populated by Al. Conversely, the higher compressibility observed for the $M2$ and $M21$ polyhedra seems to be independent of the chemistry of the site. The EoS parameters obtained with HF/DFT simulations agree with the experimental ones; only V_0 for each polyhedron is different due to the different site occupancy from the natural sample; in the simulated structure the $M1$ site is fully occupied by Mg, $M11$ by Al, $M2$ by Na, and $M21$ by Ca, leading to $Q^{\text{occ}}_{M1} = Q^{\text{occ}}_{M2} = 1$. At any rate, the $M1$ polyhedron is slightly softer than $M11$ and this is mainly due to the greater compressibility of the two bond lengths $M1$ -O11 (Fig. 5a) and $M11$ -O12 (Fig. 5b). The HP behaviour of the bond lengths within the M sites is further corroborated by the *ab initio* simulations. The experimental results show that the $M1$ -O22 bond does not decrease further above about 7 GPa. A larger deformation can be seen in the $M2$ polyhedron than in $M1$: in particular, the $M2$ -O31 bond length shows a strong decrease with pressure (Fig. 5c). For the $M21$ polyhedron the $M21$ -O32 bond length decreases more than the other bonds in this polyhedron (Fig. 5d). This significant difference may account for the greater volumetric reduction observed in the $M21$ polyhedron. Also, the $M21$ -O31 bond length does not decrease beyond 8 GPa, remaining constant up to the maximum pressure. The long $M(2,21)$ -O bond distances are related to the rotation (kinking) of the tetrahedral chain, *i.e.* the O32-O31-O32 angle between bridging oxygens in the chain, which decreases (Fig. S2; Table S4, supplementary material) from 168.5° to 164.5°: it decreases linearly to 6 GPa, remains constant up to 8 GPa, and then decreases again up to 10 GPa. The HF/DFT simulations show that this angle decreases steadily through the entire pressure range.

Deformation parameters

The pressure-induced deformation of the M sites was determined with several distortion parameters calculated with the VESTA software (Momma and Izumi, 2008), and these are reported in Table S4.

The parameter D (Baur, 1974) is based on bond lengths, and Fig. 6a shows its pressure dependence: D is higher in the $M2$ polyhedra than in $M1$ and decreases with pressure. Also, D for the $M21$ site that contains preferentially Na decreases more than D_{M2} up to ~ 6 GPa, at which pressure D values of the two polyhedra are equal. The HD/DFT results show that D_{M21} is higher than D_{M2} up to ~ 3 GPa, after which the distortion behaviour is inverted. The parameter λ (Robinson *et al.*, 1971) provides a quantitative measure of polyhedral distortion which is independent of the effective size of the polyhedron. It has been observed that λ of the $M1$ octahedron decreases with increasing pressure (Fig. 6b), but the rate of decrease begins to slow after approximately 4 GPa. The rate of decrease of λ of $M1$ octahedron calculated with *ab initio* remains relatively constant in the studied pressure range. Fig. 6c shows the pressure dependence of σ^2 (the variance of the polyhedral angles, Robinson *et al.*, 1971) of $M1$ and $M11$. The variation with pressure is antithetical for these sites. σ^2_{M1} shows a reduction from $45.34^\circ{}^2$ to $41^\circ{}^2$ at 4 GPa and remains almost constant, showing only a slight decrease at higher pressure. Instead, σ^2_{M11} remains almost constant at ca. $21^\circ{}^2$ and then starts increasing above 6 GPa, reaching almost $23^\circ{}^2$. The limited angle deformation of the $M11$ site is consistent with the higher stiffness of this polyhedron. *Ab initio* simulations confirm this behaviour: σ^2_{M1} decreases from approximately $48^\circ{}^2$ to $43^\circ{}^2$ at 8 GPa, while σ^2_{M11} exhibits a slight reduction from about $29^\circ{}^2$ to $27.7^\circ{}^2$ up to 3 GPa, after which it begins to rise, reaching $28.5^\circ{}^2$.

Discussion and conclusions

The EoS parameters from both the experimental data and the *ab-initio* calculations agree with those reported in the literature (Table 1). The values we obtained are consistent with those published by Zhang et al. (2016), although these authors derived the BM3 EoS for averaged volumes for $T1/T2$, $M1/M11$ and $M2/M21$ as the independent values were badly scattered, which they attributed to refinement artifacts. This is due to their limited reciprocal space coverage (less than 22% full coverage) and they performed refinements with restrained isotropic displacement parameters. This validation not only reinforces the reliability of our computational methods but also allows for a more detailed exploration of the baric variation of the phonon spectrum of omphacite, enhancing our understanding of the vibrational dynamics.

In situ Raman spectroscopy conducted under HP conditions on natural crystal of $Jd_{43}Di_{57}$ omphacite, described by Baratelli et al. (2024), revealed some variations in its elastic behaviour under isothermal increasing pressure conditions. The pressure dependence of some Raman peak wavenumbers exhibited anomalous behaviour near 5 GPa. Pandolfo et al. (2012), in their SC-XRD study of a sample from the same locality and of very similar composition, had observed that both $M1$ and $M11$ polyhedral volumes apparently show a slight change in slope at about 4 GPa. But the number of pressure data points and the accuracy of their refinements (limited access to reciprocal space and isotropic displacement parameters for oxygen atoms) did not allow them to draw any conclusions. This pattern has not been observed in our new dataset, where the volume of $M1$ and $M11$ octahedra remain almost constant between approximately 4.8 and 5.7 GPa, although this discrepancy may be due to the scatter of data point at 5.72 GPa. Because diffraction data with nearly complete access to reciprocal space were obtained, providing good accuracy and precision in bond lengths and angles and thus the data reliability, and because of the narrower sampling in

pressure, we had the chance to perform a comparison with the Raman results (Baratelli *et al.*, 2024). In detail, the shift of the Raman wavenumber of the peaks at 1007 and 1024 cm^{-1} shows a discontinuity close to 5 GPa, whereas the pressure dependence of the wavenumbers ($\omega(P)$) at 375 and 337 cm^{-1} shifts around 4.5 GPa, and the full width at half maximum (FWHM) of the peak at 271 cm^{-1} decreases above 5 GPa. Hybrid HF/DFT simulations revealed that the anomalous behaviour of the peak at $\sim 337 \text{ cm}^{-1}$ can be attributed to two modes of the same symmetry approaching one another in energy but without energy crossing. Within this spectral range, there are actually two A_g modes, at 337 and 349 cm^{-1} .

The 375, 349 and 337 cm^{-1} phonon modes are associated with SiO_4 tilting and M -cation vibrations, and their anomalous behaviour should be linked to a change in the M -O-Si interactions. One possible explanation is that the enhancement of phonon-phonon interactions under pressure, between 4.5 and 5 GPa, induces a homogenization of local elastic strains that are connected to the chemical ordering at the M sites. Pressure may lead to a redistribution of the local elastic strains due to the difference in the ionic sizes of the M -site cations, resulting in a tendency to unify MO_6 volumes (Fig. S3) and consequently, average effective M -O-Si force constants that appear to be the same as a state of site-occupancy disorder. This phenomenon could also be responsible for the anomaly in the averaged $\omega(P)$ of the Si-O_{nb} bond stretching modes observed near 1007 and 1024 cm^{-1} , because M -O interactions have a secondary effect on the energy of this phonon mode. The experimentally observed reduction of the FWHM of the 271- cm^{-1} peak, resulting primarily from M -cation vibrations, is also consistent with the assumption of a smaller variation in the MO_6 sizes above ~ 4.5 GPa.

The HP SC-XRD analysis conducted on an omphacite sample with the same composition

($\text{Jd}_{43}\text{Di}_{57}$) in this study has revealed a distortion variation in the $M1$ polyhedron expressed as σ^2 (Fig. 6c). This distortion is mainly influenced by the $M1\text{-O}22$ bond length (Fig. 5a), which is also associated with the TILT angle of $T2$ tetrahedron (Fig. 3b). Notably, the TILT angle of $T2$ tetrahedron stabilizes at approximately 3 GPa, which corresponds with a reduction in the rate of $M1$ polyhedron deformation. The $T2$ tetrahedron is connected to the $M1$ octahedron through the $\text{O}22$ oxygen, and the $M1\text{-O}22$ bond remains constant beyond about 7 GPa. This bond is the shortest within the $M1$ polyhedron, indicating that this distance cannot decrease beyond ~ 1.99 Å. *Ab initio* simulations indicate that the 337 cm^{-1} mode is related to the tetrahedral rotation around the c axis that can be related to the $T2$ tetrahedral TILT angle variation. Thus, both long-range (SC-XRD) and short-range (Raman spectroscopy) analysis supports the observed changes in polyhedral distortion of the $M1$ octahedra. In disordered omphacites, this behaviour cannot be observed due to symmetry constraints: in $C2/c$ omphacite, only a single $M1$ polyhedron is present, exhibiting an average chemistry between the $M1$ and $M11$ sites of $P2/n$ structure, resulting in a Raman spectrum that displays few Raman active modes.

In conclusion, for the first time, *ab-initio* calculations and accurate short-range and long-range experimental data are shown to agree in a low symmetry chemically complex mineral paving the route to a better comprehension of the complexity of the elastic behaviour in geologically important crystalline materials. By clarifying how specific vibrational modes relate to structural distortions, especially in relation to symmetry constraints and polyhedral tilting, this study enhances our ability to interpret Raman spectra in terms of atomic-scale structural changes. Furthermore, these findings have important implications not only in mineral physics, but also in metamorphic petrology. The description of the elastic and structural behaviour of omphacite crystals during compression will provide deeper insight

into the genetic processes of omphacite-rich rocks, such as eclogites, and the mechanical and seismic properties of eclogite-facies rocks, with implications for interpreting geophysical data from subduction zones and the deep crust.

Supplementary material

To view supplementary material for this article, please visit:

Acknowledgements

We thank RJ Angel for fruitful discussions that contributed to this work.

This work was funded by the Italian Ministry of University and research (MIUR) through a PhD grant to L. Baratelli and to F. Cámara and L. Baratelli through the project “Dipartimenti di Eccellenza 2023-2027”. This work was financially supported by the Fondazione Cariplo grant agreement #2023-2431 assigned to M. Alvaro by the PRIN-MUR project no. 2020WPMFE9 to G. Pennacchioni and no. 2022AL5MSN to M. Cremonesi.

Competing interests: the authors declare none.

References

- Angel, R.J. (2000) 2. Equations of State. Pp. 35–60 in: *High-Temperature and High Pressure Crystal Chemistry*. De Gruyter.
- Angel, R.J., Downs, R.T. and Finger, L.W. (2000) High-Temperature-High- Pressure Diffraction. *Reviews in Mineralogy and Geochemistry*, **41**, 559–597.
- Angel, R.J., Bujak, M., Zhao, J., Gatta, G.D. and Jacobsen, S.D. (2007) Effective hydrostatic limits of pressure media for high-pressure crystallographic studies. *Journal of Applied Crystallography*, **40**, 26–32.
- Angel, R.J., Mazzucchelli, M.L., Baratelli, L., Schweinle, C.F., Balic-Zunic, T., Gonzalez-Platas, J. and Alvaro, M. (2025) Uncertainties of recalculated bond lengths, angles and polyhedral volumes as implemented in the Crystal Palace program for parametric crystal structure analysis. *Acta Crystallographica A*, **81**(3), 202–210.
- Baratelli, L., Murri, M., Alvaro, M., Prencipe, M., Mihailova, B. and Cámara, F. (2024) Raman scattering of omphacite at high pressure: towards its possible application to elastic geothermobarometry. *American Mineralogist*, **109**, 2105–2115.
- Baur, W.H. (1974) The geometry of polyhedral distortions. Predictive relationships for the phosphate group. *Acta Crystallographica Section B Structural Crystallography and Crystal Chemistry*, **30**, 1195–1215.
- Bhagat, S.S., Bass, J.D. and Smyth, J.R. (1992) Single-crystal elastic properties of omphacite-C2/c by Brillouin spectroscopy. *Journal of Geophysical Research*, **97**, 6843–6848.
- Boffa Ballaran, T., Carpenter, M.A., Domeneghetti, M.C. and Tazzoli, V. (1998a) Structural mechanisms of solid solution and cation ordering in augite-jadeite pyroxenes: I. A macroscopic perspective. *American Mineralogist*, **83**, 419–433.

- Boffa Ballaran, T., Carpenter, M.A., Domeneghetti, M.C., Salje, E.K.H. and Tazzoli, V. (1998b) Structural mechanisms of solid solution and cation ordering in augite-jadeite pyroxenes: II. A microscopic perspective. *American Mineralogist*, **83**, 434–443.
- Cámara, F., Nieto, F. and Oberti, R. (1998) Effects of Fe²⁺ and Fe³⁺ contents on cation ordering in omphacite. *European Journal of Mineralogy*, **10**, 889–906.
- Cameron, M., Sueno, S., Prewitt, C.T. and Papike, J.J. (1973) High temperature crystal chemistry of acmite, diopside, hedenbergite, jadeite, spodumene, and ureyite. *American Mineralogist*, **58**, 594–618.
- Carpenter, M.A., Domeneghetti, M.-C. and Tazzoli, V. (1990a) Application of Landau theory to cation ordering in omphacite I: Equilibrium behaviour. *European Journal of Mineralogy*, **2**, 7–18.
- Carpenter, M.A., Domeneghetti, M.-C. and Tazzoli, V. (1990b) Application of Landau theory to cation ordering in omphacite II: Kinetic behaviour. *European Journal of Mineralogy*, **2**, 19–28.
- Civalleri, B., D'Arco, Ph., Orlando, R., Saunders, V.R. and Dovesi, R. (2001) Hartree–Fock geometry optimisation of periodic systems with the Crystal code. *Chemical Physics Letters*, **348**, 131–138.
- Dovesi, R., Erba, A., Orlando, R., Zicovich-Wilson, C.M., Civalleri, B., Maschio, L., Rérat, M., Casassa, S., Baima, J., Salustro, S. and Kirtman, B. (2018) Quantum-mechanical condensed matter simulations with CRYSTAL. *WIREs Computational Molecular Science*, **8**.
- Ghignone, S., Prencipe, M., Manzotti, P., Bruno, M., Boero, F., Borghini, A., Costa, E., Ciriotti, M. and Scaramuzzo, E. (2024) The Raman spectrum of florencite-(REE) [REEAl₃(PO₄)₂(OH)₆]: An integrated experimental and computational approach. *Journal*

of Raman Spectroscopy, **55**, 394–405.

Gonzalez-Platas, J., Alvaro, M., Nestola, F. and Angel, R. (2016) *EosFit7-GUI: a new graphical user interface for equation of state calculations, analyses and teaching. Journal of Applied Crystallography*, **49**, 1377–1382.

Hao, M., Zhang, J.S., Pierotti, C.E., Ren, Z. and Zhang, D. (2019) High-Pressure Single-Crystal Elasticity and Thermal Equation of State of Omphacite and Their Implications for the Seismic Properties of Eclogite in the Earth's Interior. *Journal of Geophysical Research: Solid Earth*, **124**, 2368–2377. Blackwell Publishing Ltd.

Hawthorne, F.C., Ungaretti L. and Oberti R. (1995) Site populations in minerals: terminology and presentation of results of crystal-structure refinement. *Canadian Mineralogist*, **33**, 907–911.

Klotz, S., Chervin, J.C., Munsch, P. and Le Marchand, G. (2009) Hydrostatic limits of 11 pressure transmitting media. *Journal of Physics D: Applied Physics*, **42**.

Lee, C., Yang, W. and Parr, R.G. (1988) Development of the Colle-Salvetti correlation-energy formula into a functional of the electron density. *Physical Review B*, **37**, 785–789.

Mao, H.K., Xu, J. and Bell, P.M. (1986) Calibration of the ruby pressure gauge to 800 kbar under quasi-hydrostatic conditions. *Journal of Geophysical Research: Solid Earth*, **91**, 4673–4676.

Matthes, S. and Schmidt, K. (1974) Eclogites of the Münchberg Mass, NE Bavaria. *Fortschritte der Mineralogie*, **52**, 33–57.

McCormick, T.C., Hazen, R.M. and Angel, R.J. (1989) Compressibility of omphacite to 60 kbar: Role of vacancies. *American Mineralogist*, **74**, 1287–1292.

Momma, K. and Izumi, F. (2008) *VESTA: a three-dimensional visualization system for*

- electronic and structural analysis. *Journal of Applied Crystallography*, **41**, 653–658.
- Monkhorst, H.J. and Pack, J.D. (1976) Special points for Brillouin-zone integrations. *Physical Review B*, **12**, 5188–5193.
- Nishihara, Y., Takahashi, E., Matsukage, K. and Kikegawa, T. (2003) Thermal equation of state of omphacite. *American Mineralogist*, **88**, 80–86.
- O'Brien, P.J. (1993) Partially retrograded eclogites of the Munchberg Massif, Germany: records of a multi-stage Variscan uplift history in the Bohemian Massif. *Journal of Metamorphic Geology*, **11**, 241–260.
- Pandolfo, F., Nestola, F., Cámara, F. and Domeneghetti, M.C. (2012a) High-pressure behavior of space group P2/n omphacite. *American Mineralogist*, **97**, 407–414. Walter de Gruyter GmbH.
- Pandolfo, F., Nestola, F., Cámara, F. and Domeneghetti, C. (2012b) New thermoelastic parameters of natural C2/c omphacite. *Physics and Chemistry of Minerals*, **39**, 295–304. Springer Verlag.
- Pavese, A., Bocchio, R. and Ivaldi, G. (2000) In situ high temperature single crystal X-ray diffraction study of a natural omphacite. *Mineralogical Magazine*, **64**, 983–993.
- Pavese, A., Diella, V., Levy, D. and Hanfland, M. (2001) Synchrotron X-ray powder diffraction study of natural P2/n-omphacites at high-pressure conditions. *Physics and Chemistry of Minerals*, **28**, 9–16.
- Petříček, V., Dušek, M. and Palatinus, L. (2014) Crystallographic Computing System JANA2006: General features. *Zeitschrift für Kristallographie - Crystalline Materials*, **229**, 345–352.
- Prencipe, M. (2012) Simulation of vibrational spectra of crystals by ab initio calculations: An invaluable aid in the assignment and interpretation of the Raman

signals. the case of jadeite ($\text{NaAlSi}_2\text{O}_6$). *Journal of Raman Spectroscopy*, **43**, 1567–1569.

John Wiley and Sons Ltd.

Prencipe, M. (2019) Quantum mechanics in Earth sciences: a one-century-old story.

Rendiconti Lincei, **30**, 239–259. Springer-Verlag Italia s.r.l.

Prencipe, M., Scanavino, I., Nestola, F., Merlini, M., Civalleri, B., Bruno, M. and Dovesi,

R. (2011) High-pressure thermo-elastic properties of beryl ($\text{Al}_4\text{Be}_6\text{Si}_{12}\text{O}_{36}$) from ab initio

calculations, and observations about the source of thermal expansion. *Physics and*

Chemistry of Minerals, **38**, 223–239.

Prencipe, M., Mantovani, L., Tribaudino, M., Bersani, D. and Lottici, P.P. (2012) The

Raman spectrum of diopside: a comparison between ab initio calculated and

experimentally measured frequencies. *European Journal of Mineralogy*, **24**, 457–464.

Schweizerbart.

Rigaku Oxford Diffraction. (2019) CrysAlisPro Software system, version 1.171.40.53.

Rigaku Corporation, Oxford, UK.

Robinson, K., Gibbs, G. V. and Ribbe, P.H. (1971) Quadratic Elongation: A Quantitative

Measure of Distortion in Coordination Polyhedra. *Science*, **172**, 567–570.

Sheldrick, G.M. (2015) Crystal structure refinement with SHELX. *Acta Crystallographica*,

C71, 3–8.

Sophia, G., Baranek, P., Sarrazin, C., Rérat, M. and Dovesi, R. (2014) Systematic

influence of atomic substitution on the phase diagram of ABO_3 ferroelectric

perovskites. https://www.crystal.unito.it/Basis_Sets/tin.html.

Stangarone, C., Tribaudino, M., Prencipe, M. and Lottici, P.P. (2016) Raman modes in

Pbca enstatite ($\text{Mg}_2\text{Si}_2\text{O}_6$): an assignment by quantum mechanical calculation to

interpret experimental results. *Journal of Raman Spectroscopy*, **47**, 1247–1258.

Valenzano, L., Torres, F.J., Doll, K., Pascale, F., Zicovich-Wilson, C.M. and Dovesi, R. (2006) *Ab Initio* Study of the Vibrational Spectrum and Related Properties of Crystalline Compounds; the Case of CaCO₃ Calcite. *Zeitschrift für Physikalische Chemie*, **220**, 893–912.

Wilson, A.J.C. (1995) International Tables for Crystallography. P. in: *International Tables for Crystallography*. Kluwer Academic Publishers, Dordrecht.

Wu, Z. and Cohen, R.E. (2006) More accurate generalized gradient approximation for solids. *Physical Review B*, **73**, 235116.

Xu, J., Zhang, D., Fan, D., Dera, P.K., Shi, F. and Zhou, W. (2019) Thermoelastic Properties of Eclogitic Garnets and Omphacites: Implications for Deep Subduction of Oceanic Crust and Density Anomalies in the Upper Mantle. *Geophysical Research Letters*, **46**, 179–188.

Ye, Z., Fan, D., Li, B., Tang, Q., Xu, J., Zhang, D. and Zhou, W. (2022) Thermal equation of state of the main minerals of eclogite: Constraining the density evolution of eclogite during the delamination process in Tibet. *Solid Earth*, **13**, 745–759.

Zhang, D., Hu, Y. and Dera, P.K. (2016) Compressional behavior of omphacite to 47 GPa. *Physics and Chemistry of Minerals*, **43**, 707–715. Springer Verlag.

1 **Table 1.** EoSs of omphacite from literature.

2

	McCormick <i>et al.</i> , 1989*	McCormick <i>et al.</i> , 1989**	Pavese <i>et al.</i> , 2000, 2001	Nishihara <i>et al.</i> , 2003	Pandolfo <i>et al.</i> , 2012a	Pandolfo <i>et al.</i> , 2012b	Zhang <i>et al.</i> , 2016	Xu <i>et al.</i> , 2019	Xu <i>et al.</i> , 2019	Ye <i>et al.</i> , 2022
Space group	<i>C2/c</i>	<i>C2/c</i>	<i>P2/n</i>	<i>C2/c</i>	<i>P2/n</i>	<i>C2/c</i>	<i>P2/n</i>	<i>C2/c</i>	<i>P2/n</i>	***
Di (wt%)	30.6	37.7	47.4	63	48.0	48.0	51.5	-	-	-
Jd (wt%)	69.4	62.3	46.4	37	52.0	52.0	46.5	42	27	45
Ae (wt%)	-	-	6.2	-	-	-	2.0	1	20	7
Quad (wt%)	-	-	-	-	-	-	-	57	53	48
P-V EoS	BM2	BM2	BM3	BM2	BM3	BM3	BM3	BM2	BM3	BM3
K_0 (GPa)	129(3)	139(4)	117(3)	126(1)	122(1)	119(2)	116(2)	123.6(5)	115(2)	121(2)
K'	4.0	4.0	6.0(1)	4.0	5.1(3)	5.7(6)	4.3(2)	4.0	4.9(4)	3.90(35)
V_0 (Å ³)	411.7(1)	414.3(3)	422.2(1)	423.8	421.43(4)	421.04(7)	423.9(3)	422.3(1)	426.0(2)	423.48(24)
T-V EoS	-	-	Vinet <i>et al.</i> (1987b)	HTBM	-	Berman (1988)	-	HTBM	HTBM	Holland and Powell (2011)
α_V (10 ⁻⁵ K ⁻¹)	-	-	2.76(4)	2.2(1)	-	2.64(2)	-	2.8(3)	3.4(4)	3.73(20)
$\partial K_T/\partial T$ (GPa/K)	-	-	-	-0.015(4)	-	-	-	-0.011(5)	-0.009(6)	-
Q_{M1}	-	-	0.84	-	0.8956	-	0.81	-	***	***
Q_{M2}	-	-	0.42	-	0.4993	-	0.39	-	***	***
P (GPa)	0-6	0-6	0-13	0-10	0-7.5	0-7	0-47	0-24	0-24	0-25.6
T (°C)	25	25	25-1000	25-727	25	25-800	25	25-427	25-427	25-427

Chemical composition, EoSs type, bulk modulus K_0 , its pressure derivative K' , the zero-pressure volume V_0 , thermal expansion α_V , the bulk modulus temperature derivative $\partial K_T/\partial T$, as well as the order parameters Q_{M1} and Q_{M2} , pressure and temperature conditions are listed for each study.

*Vacancy-rich omphacite; **vacancy-poor omphacite.

*** not reported.

Note: For Zhang *et al.* (2016) Q_{M2} is calculated based on the site occupancy factor, while Q_{M1} as a function of the bond distances (Carpenter *et al.* 1990a).

Note: In Xu *et al.* (2019) and Ye *et al.* (2022) the composition Quad is defined as ferrosilite + enstatite + wollastonite.

3

4

5 **Table 2.** Site populations and degree of order of the analysed $Jd_{43}Di_{57}$ omphacite.
6

<i>T1</i>	Si	1	<i>T2</i>	Si	0.9709(10)
				Al	0.0291(10)
<i>M1</i>	Mg	0.868(2)	<i>M2</i>	Ca	0.3621(17)
	Al	0.045(2)		Na	0.6378(17)
	Fe ²⁺	0.087(2)			
<i>M11</i>	Mg	0.088(2)	<i>M21</i>	Ca	0.7903(17)
	Al	0.860(2)		Na	0.2096(17)
	Fe ²⁺	0.052(2)			
Q_{M1}^{occ}		0.822(13)	Q_{M2}^{occ}		0.438(10)
Q_{M1}^{dist}		0.0645(5)	Q_{M2}^{dist}		0.0151(4)

7 Note: order parameters calculated following Carpenter et al. (1990a)

Prepublished article

8 **Table 3.** Unit-cell parameters at different pressures of omphacites.

9

	$P(\text{GPa})$	$a(\text{\AA})$	$b(\text{\AA})$	$c(\text{\AA})$	$\beta(^{\circ})$	$V(\text{\AA}^3)$
Observed	In air	9.5882(2)	8.7847(1)	5.2580(1)	106.835(2)	423.898(14)
	0.88(15)	9.559(4)	8.744(5)	5.2389(13)	106.70(4)	419.4(3)
	1.06(1)	9.544(3)	8.758(4)	5.2341(10)	106.76(3)	418.9(3)
	1.20(1)	9.546(3)	8.753(3)	5.2352(7)	106.74(2)	418.9(2)
	1.58(2)	9.543(4)	8.738(4)	5.2297(10)	106.73(3)	417.6(3)
	1.95(7)	9.528(4)	8.731(5)	5.2243(10)	106.65(3)	416.4(3)
	2.32(10)	9.516(4)	8.715(5)	5.2174(12)	106.63(4)	414.6(3)
	2.70(11)	9.508(3)	8.707(5)	5.2129(9)	106.60(3)	413.6(3)
	3.25(7)	9.496(5)	8.694(6)	5.2067(12)	106.54(4)	412.1(4)
	4.24(2)	9.479(4)	8.672(5)	5.1963(10)	106.45(3)	409.7(3)
	4.30(2)	9.475(4)	8.670(4)	5.1953(9)	106.44(3)	409.3(3)
	4.45(7)	9.473(4)	8.661(5)	5.1911(10)	106.43(3)	408.5(3)
	4.86(6)	9.462(3)	8.649(4)	5.1860(9)	106.39(3)	407.1(2)
	5.18(12)	9.458(3)	8.642(4)	5.1852(8)	106.35(3)	406.7(2)
	5.72(16)	9.449(4)	8.635(5)	5.1782(10)	106.31(3)	405.5(3)
	6.19(15)	9.432(4)	8.618(5)	5.1704(10)	106.26(3)	403.5(3)
	7.11(6)	9.417(3)	8.600(4)	5.1603(8)	106.17(3)	401.4(2)
	8.04(7)	9.397(3)	8.577(4)	5.1488(9)	106.11(3)	398.7(2)
	8.46(9)	9.389(4)	8.571(5)	5.1405(9)	106.05(3)	397.5(3)
	8.61(6)	9.386(3)	8.561(4)	5.1412(8)	106.07(3)	397.0(2)
9.13(8)	9.388(3)	8.536(4)	5.1375(8)	105.93(2)	395.9(2)	
9.73(1)	9.361(4)	8.555(3)	5.1228(12)	106.08(4)	394.2(3)	
HF/DFT calculated	-2	9.677	8.838	5.320	107.57	433.7
	-1	9.645	8.809	5.303	107.39	429.9
	0	9.614	8.781	5.287	107.22	426.3
	1	9.586	8.754	5.271	107.06	422.8
	2	9.559	8.727	5.256	106.92	419.5
	3	9.534	8.702	5.241	106.78	416.3
	4	9.510	8.678	5.227	106.65	413.3
	5	9.488	8.654	5.213	106.54	410.3
	6	9.467	8.631	5.200	106.43	407.5
7	9.446	8.609	5.187	106.33	404.8	
8	9.427	8.588	5.175	106.24	402.2	

10

11

12 **Table 4.** EoS parameters of omphacites determine din this study.

13

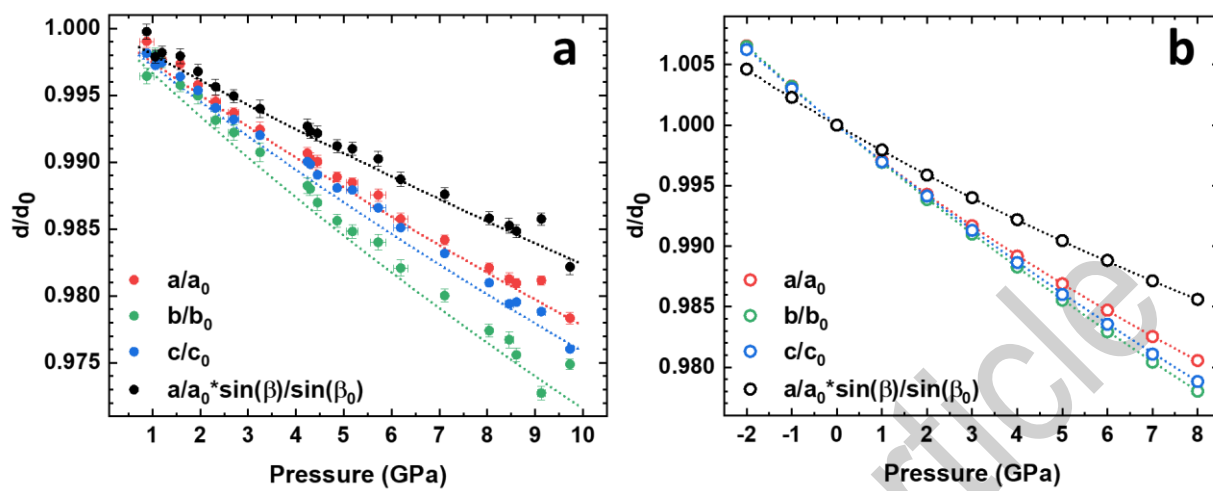
	Observed (BM2 EoS)		HF/DFT calculated (BM3 EoS)		
	Parameters	K_0 (GPa)	Parameters	K_0 (GPa)	K'
a_0 (Å)	9.5744(19)	130(7)	9.61401(17)	109(1)	7.5(5)
b_0 (Å)	8.786(4)	97(7)	8.78069(16)	106(1)	3.8(4)
c_0 (Å)	5.2526(10)	118(6)	5.28671(11)	110(2)	4.0(4)
$a_0 \cdot \sin\beta$ (Å)	9.163(3)	168(14)	9.18334(14)	154(2)	8.3(8)
V_0 (Å ³)	422.85(15)	121.3(1.2)	426.52(3)	119(2)	4.9(5)
V_{M1} (Å ³)	11.693(19)	109(5)	11.8117(13)	104.4(7)	5.1(3)
V_{M11} (Å ³)	9.708(18)	144(8)	9.5521(3)	137.8(3)	5.96(11)
V_{M2} (Å ³)	24.78(3)	93(3)	25.089(10)	91(2)	3.4(6)
V_{M21} (Å ³)	26.02(3)	89(2)	25.779(4)	93.9(7)	4.3(3)

14

15

Prepublished article

16 **Figure 1.** Evolution of the (a) experimentally observed and (b) *ab initio* calculated unit-cell
17 parameters.

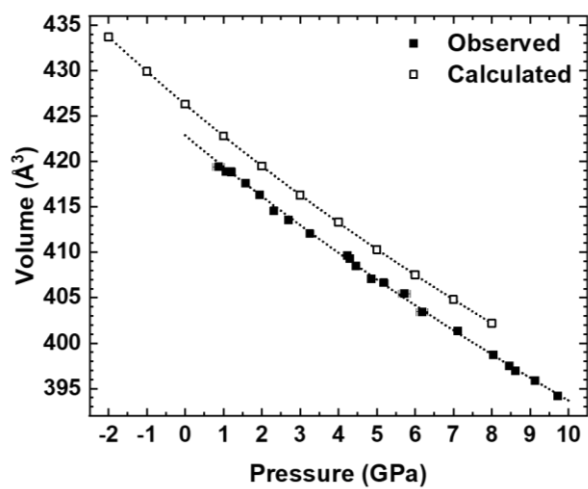


18

19

Prepublished article

20 **Figure 2.** Evolution the unit-cell volume with pressure of the analysed crystal ($\text{Jd}_{43}\text{Di}_{57}$) compared
21 to the HF/DFT calculated one ($\text{Jd}_{50}\text{Di}_{50}$).

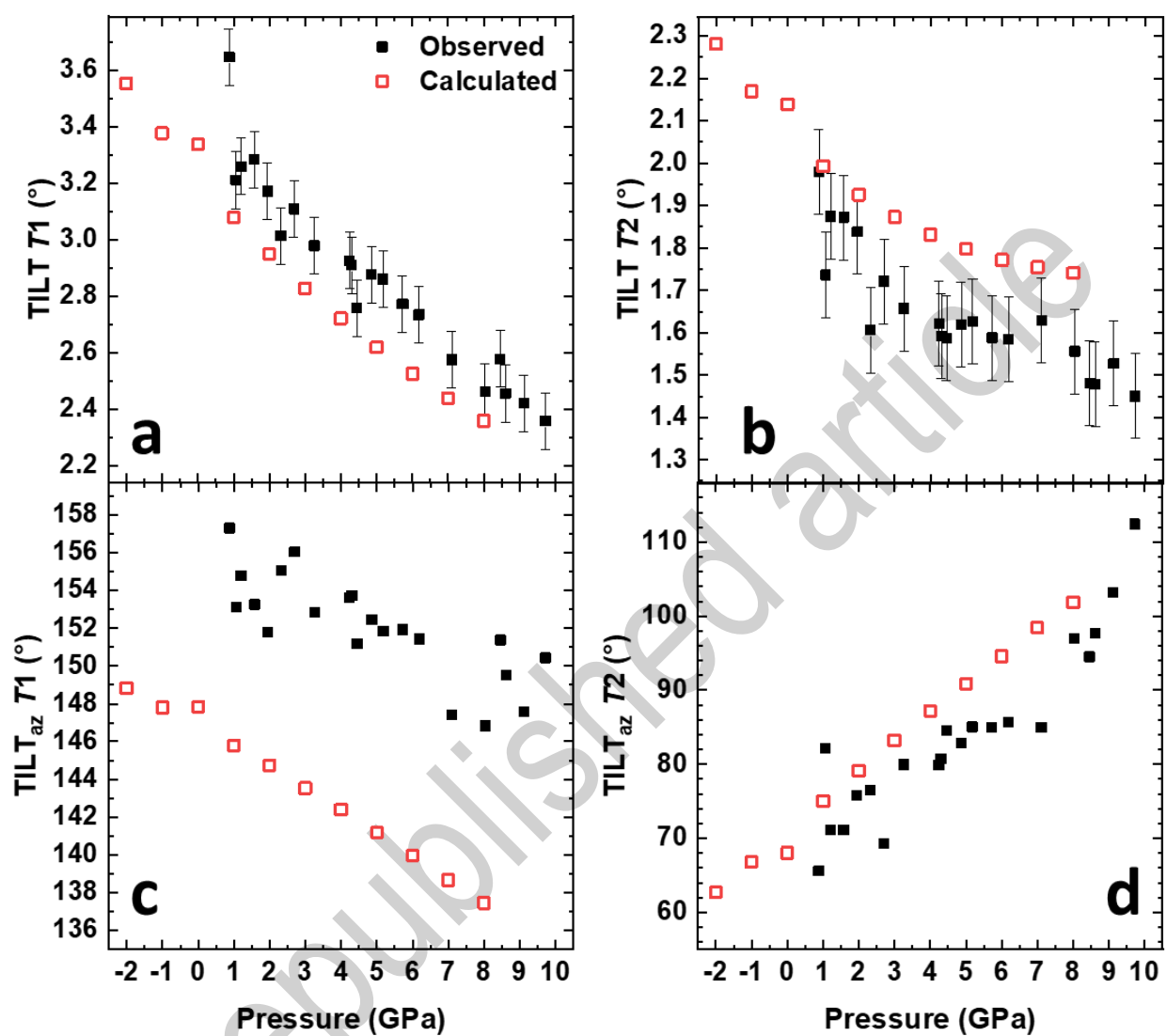


22

23

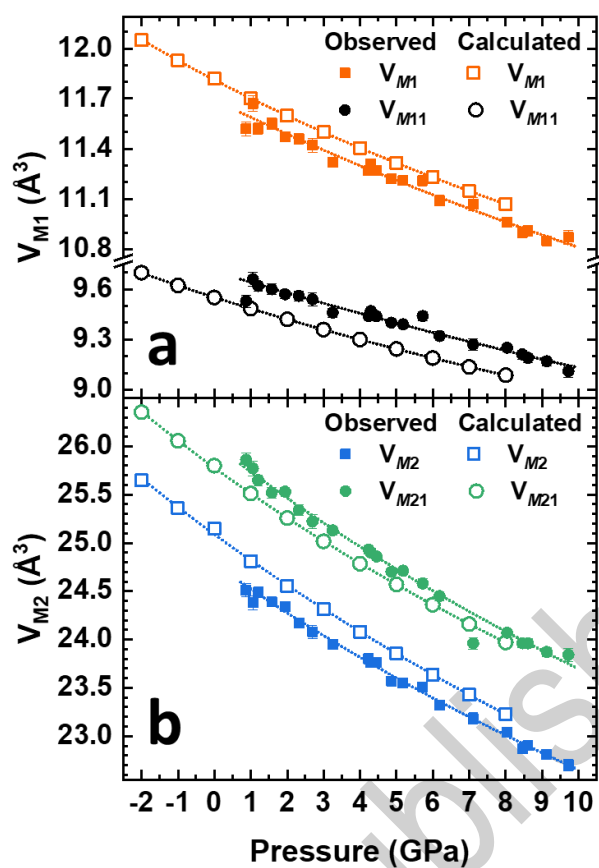
Prepublished article

24 **Figure 3.** Pressure dependence of the TILT angle related to (a) T_1 and (b) T_2 , and the TILT_{az} angle
25 related to (c) T_1 and (d) T_2 . The data are compared to the ones obtained with HF/DFT simulations.



26
27

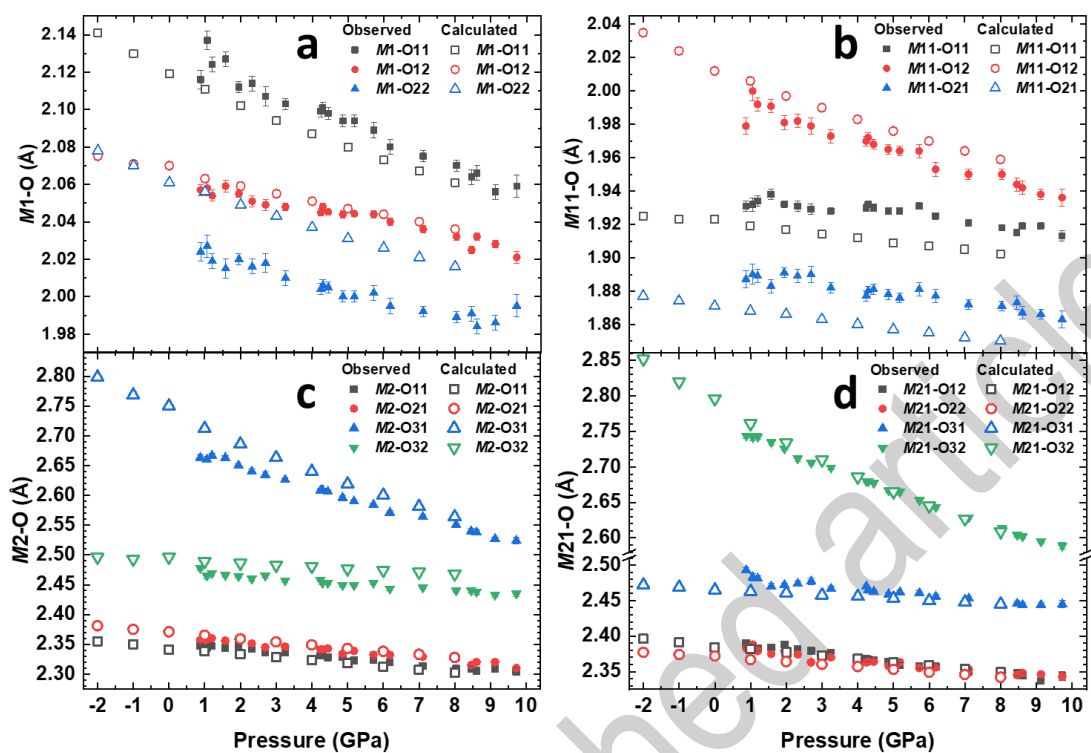
28 **Figure 4.** Variation of (a) $M1$ and $M11$, and (b) $M2$ and $M21$ polyhedral volumes as a function of
29 pressure, compared to the correspondent polyhedral volumes calculated by *ab initio* simulations.
30 $M1$ is preferentially occupied by Mg, $M11$ by Al, $M2$ by Na, and $M21$ by Ca.



31

32

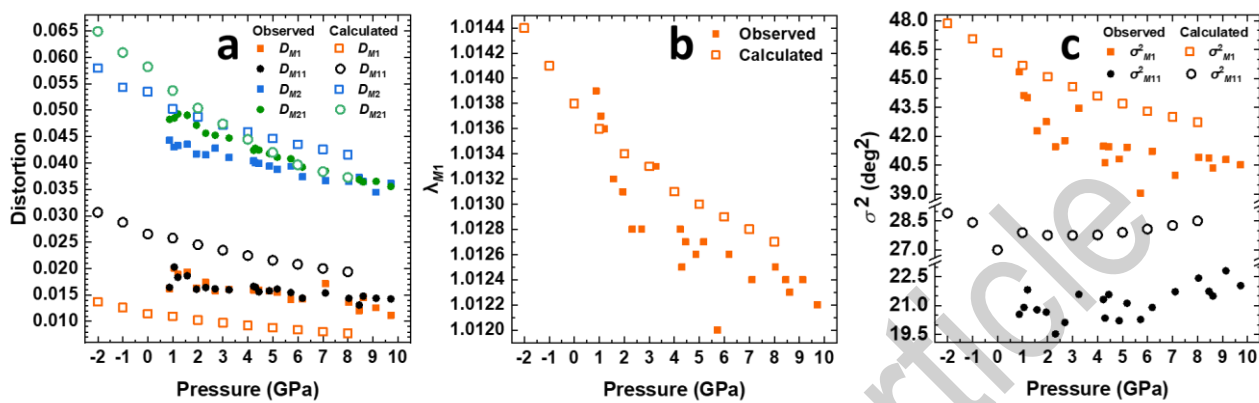
33 **Figure 5.** Pressure dependence of the bond lengths of the six- and eight-coordinated sites
34 compared to the ones calculated by HF/DFT: (a) *M1*; (b) *M11*; (c) *M2*; (d) *M21* bond lengths.



35

36

37 **Figure 6.** Pressure dependence of (a) the distortion index D (Baur, 1974) of the six- and eight-
38 coordinated sites, (b) the quadratic elongation λ (Robinson *et al.*, 1971) of $M1$, and (c) bond angle
39 variance σ^2 (Robinson *et al.*, 1971) of $M1$ and $M11$.



40

41

Prepublished article